Journal of Ultrafine Grained and Nanostructured Materials
https://jufgnsm.ut.ac.ir
Vol. 58, No.2, June 2025, pp. 255-263
Print ISSN: 2423-6845 Online ISSN: 2423-6837
DOI: 10.22059/jufgnsm.2025.02.10

Effect of hydrogen peroxide on crystalline orientation and optoelectrical properties of aluminum-doped zinc oxide prepared by chemical bath deposition

Parvin Asen[a], Maryam Heidariramsheh*[b], Parvin Abachi[c], Nima Taghavinia[d]

[a] Department of Nano Biotechnology, Faculty of Biotechnology, Amol University of Special Modern Technologies, Amol 46158-63111, Iran
[b] School of Metallurgy and Materials Engineering, College of Engineering, University of Tehran, P.O. Box 11155-4563, Tehran, Iran
[c] Department of Materials Science and Engineering, Sharif University of Technology, Azadi Avenue, Tehran, 14588, Iran
[d] Nanoparticles and Coatings Lab, Department of Physics, Sharif University of Technology, Tehran, 14588, Iran

Recieved: 28 June 2025; Accepted: 18 September 2025

*Corresponding author, E-mail: m.heidariramsheh@ut.ac.ir

ABSTRACT

The current work demonstrates the growth of aluminum-doped ZnO (AZO) hexagonal rods vertically aligned on soda-lime glass (SLG) via the chemical bath deposition (CBD) method. The controlling crystalline orientation was performed using hydrogen peroxide (H_2O_2) accompanied by $C_6H_{17}N_3O_7$ as growth controlling agents (CAs). The results showed that the presence of H_2O_2 significantly promoted (002) plane orientation and significantly improved structural, morphological, and optical properties of AZO. The as-fabricated AZO with H_2O_2 exhibited a layer thickness of 1.8 µm, optical transparency of 90.4 %, sheet resistance of 10 Ω $\square^{-1}$ and the resistivity of 1.8×10^{-3} Ω.cm. This approach provides an efficient route to alter the AZO morphology and properties for advanced optoelectronic applications.

Keywords: *Transparent Conductive Oxide, Aluminum-doped zinc oxide, Chemical Bath deposition, Controlling agent, H_2O_2.*

1. Introduction

In optoelectronic devices, front and back contact electrodes serve to collect current or apply bias, with various types optimized for specific applications. These electrodes can be transparent, metallic, or conductive polymer-based, and their choice impacts device performance in terms of transparency, conductivity, and stability [1, 2]. Recent advancements in opto-electronic applications and growing consumer interest in these products have generated substantial market demand for transparent conductive oxides (TCOs). TCOs are ideal for utilizing photovoltaic devices and flat panel displays due to their high optical transparency and electrical conductivity. One of the most popular TCO materials is indium tin oxide (ITO) because of its high optical transmittance and good electrical conductivity. Nevertheless, the limited supply of indium and the high cost of preparation drive researchers to investigate new alternatives. Some transparent TCOs, such as zinc oxide (ZnO) [3], titanium dioxide (TiO_2) [4], and tin oxide (SnO_2) [5], have been supposed as potential substitutes for ITO. Among these materials, ZnO has attracted considerable attention owing to its abundance, cost-effectiveness, and non-toxicity.

ZnO can function as either an n-type or a p-type semiconductor depending on the dopant used. N-type dopants typically include elements from the scandium (Sc) family (group 3), the boron (B) family (group 13), the carbon (C) family (group 14), and the halogens (group 17). For TCO based on ZnO, the process of n-type doping is more straightforward than that of p-type doping. For the TCO application, the doping of ZnO with group 13 elements, e.g., B, aluminum (Al), gallium (Ga), and indium (In), was conducted to improve its electrical conductivity [6-9]. Among these elements, Al offers unique benefits compared to other doping materials owing to its low cost, non-toxic nature, low electrical resistivity, and exceptional transparency in both the visible and near-infrared spectral regions [10]. Hence, Al-doped ZnO (AZO) is considered as an attractive low-cost material for TCO applications. There are several techniques available for the fabrication of AZO films, including magnetron sputtering, spin coating, vacuum vapor deposition, sol-gel ultrasonic spray pyrolysis, atomic layer deposition (ALD), and chemical bath deposition (CBD) [11-14]. Among them, the CBD approach is preferred over other methods due to its advantages, such as low cost, simple application, and easy change of parameters (e.g., precursor concentration, deposition time, temperature, and pH), without the need for additional annealing [15]. Therefore, the development of fabrication methods effectively influences the tuning of AZO film structure, thereby affecting the properties of AZO, such as conductivity and transparency. In addition, adjusting the crystallographic orientation through controlling agents (CAs) is another critical variable to change the optical and electrical properties [16]. So far, various CAs have been used for the synthesis of ZnO or AZO films, such as urea [17], ethylenediamine [18], dimethylamineborane (DMAB) [19], triethanolamine [20], etc. However, widespread research is focused on new CA for producing AZO films with high transparency and conductivity.

The purpose of this study is to investigate the CA effects of H_2O_2 and $C_6H_{17}N_3O_7$ on the optical and electrical conductivity of AZO. Hence, we successfully deposited crystalline vertically aligned AZO rods using the CBD method on soda-lime glass (SLG), and the structure, morphology, and optical characteristics of AZO films were studied.

2. Experimental section

2.1. chemicals

Zinc oxide (ZnO, Sigma-Aldrich 99 %), ammonia (NH_3 (aq), Merck 99 %), hydrochloric acid (HCl, Merck 37 %), hydrogen peroxide (H_2O_2, Merck 30 %) isopropyl alcohol (C_3H_8O, Merck 99 %), triammonium citrate ($C_6H_{17}N_3O_7$, Merck 99%), ammonium nitrate (NH_4NO_3, Merck 99 %), and aluminum hydroxide ($Al(OH)_3$, Merck 99 %), were used as received without any further purification.

2.2. Preparation of Seed Layer on SLG

Prior to the deposition of the seed layer, the glass surface was polished by a soft toothbrush. Subsequently, the glass was cleaned ultrasonically in a detergent solution, 0.1 M HCl, isopropyl alcohol, and deionized water (DI) water successively for 2, 15, 15, and 2 minutes, respectively. Then, the pre-cleaned glass substrate was dried with dry air and heated in the oven at 500 °C for 1 h to remove the remaining contaminants. Thereafter, the ZnO seed layer covered the substrate from the bath solution containing 50 mM ZnO and 5 M $NH_{3\,(aq)}$ via the spin coating technique at a rotation speed of 3000 rpm for 30 s. After deposition, the sample was thoroughly rinsed with DI water to remove loosely adhered particles from the surface and dried at 100 °C for 5 min.

2.3. AZO Deposition

AZO was prepared on the deposited seed layer/SLG through the CBD technique. The solution of 50 mM ZnO, 50 mM $C_6H_{17}N_3O_7$, 50 mM NH_4NO_3, and 1 mM NH_3 (named "A") was stirred for 24 hours. The mixture was filtered to eliminate residual ZnO particles, resulting in a completely transparent solution. The as-prepared solution was heated at 85°C and stirred for 15 min. Thereafter, the as-fabricated substrate was soaked in the chemical bath for 40 min. Thus, the pristine ZnO was synthesized on the seed layer-coated SLG. To prepare the AZO films using H_2O_2, the solution containing "A", 3 mM of $Al(OH)_3$ precursor, and 3 mM H_2O_2 was stirred for 3 h at 25°C and then stored in the refrigerator for 24 h. Then, a similar approach was performed for the deposition of AZO. After that, the AZO layer was immersed in an ultrasonic bath for 10 minutes to remove any agglomerate particles on its surface, followed by drying in an oven at 100 °C. The as-prepared layer was exposed to ultraviolet (UV) light from a 400 W lamp inside a closed chamber for 20 min. As $C_6H_{17}N_3O_7$ is also a CA, for comparison, a similar approach was performed for the deposition of AZO without using $C_6H_{17}N_3O_7$ and H_2O_2.

2.4. Characterization techniques

The electric sheet resistance (ρ) was measured using a 4-point probe and calculated using the following equation:

$$\rho = \frac{\pi}{\ln(2)} \frac{V}{I} \quad (1)$$

V denotes the voltage between the two inner probes, I represents the current through the initial and final probes, and π/Ln2 is the constant number of 4.53. Furthermore, the bulk resistivity of the film can also be calculated by multiplying ρ by the film thickness (t) as shown by equation (2):

$$\rho = \frac{\pi}{\ln(2)}\left(\frac{V}{I}\right) t = 4.532\left(\frac{V}{I}\right) t \quad (2)$$

The X-ray diffraction (XRD) patterns were obtained using a PANalytical X'Pert Pro MPD X-ray diffractometer with Cu Kα radiation (λ = 1.54). Field emission scanning electron microscopy (FE-SEM: TESCAN MIRA3 XMU) was employed to investigate the morphology of the samples. The optical transmission and absorption spectra were recorded using a UV-Vis spectrophotometer (PerkinElmer Lambda 25).

3. Results and discussion

The schematic preparation of AZO thin film is illustrated in Fig.1a. To synthesize the vertically aligned AZO via the CBD approach, a ZnO seed layer is usually deposited on a cleaned substrate due to the reduction of the thermodynamic barrier (heterogeneous nucleation) and generation of nucleation centers . Hence, it was prepared by spin coating on SLG. The proposed reaction mechanism for the formation of the ZnO seed layer is:

$$C_6H_{17}N_3O_7 \Leftrightarrow C_6H_8O_7 + 3NH_3 \quad (3)$$

$$ZnO_{(s)} + xNH_3 + zOH^- + H_2O \rightarrow [Zn(NH_3)_3(OH)_y]^{(2+)-y} + (2+z-y)(OH)^- \quad (4)$$

One of the important steps to achieve better transparency is the ultrasonic bath treatment process to remove the particles accumulated on the surface of the layer [21, 22]. Interestingly, these very large aggregates, as seen in Fig.2, are a combination of ZnO, which is doped with Al in higher amounts than the bulk layer. The presence of these aggregates has a significant effect on the transparency of the layers due to light scattering, while it does not have a significant effect on sheet resistance [23, 24].

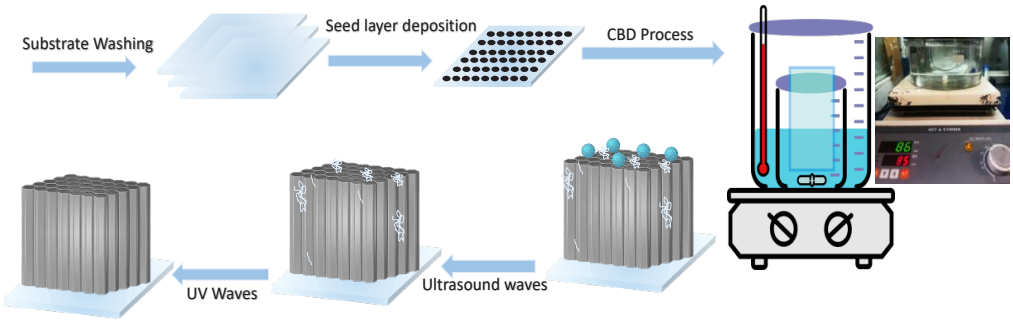

Fig. 1- The deposition of AZO films via the CBD method, followed by three post-deposition treatments: sonication, drying, and UV irradiation.

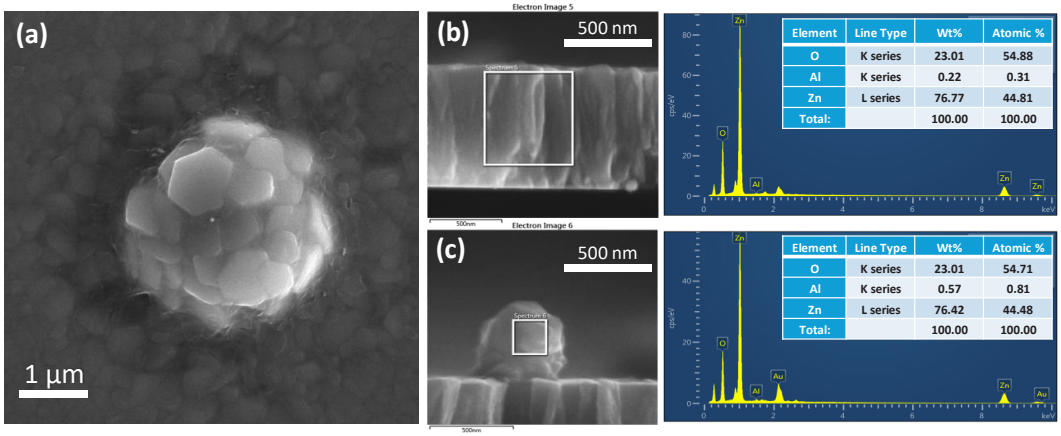

Fig. 2- (a) The FESEM of deposited AZO layer and agglomerated particulates on the surface (b,c) The chemical composition in cross section of deposited AZO layer and agglomerated particulate on the AZO surface.

The XRD patterns of prepared AZO without CAs, and with $C_6H_{17}N_3O_7$, as well as $C_6H_{17}N_3O_7$+H_2O_2, are shown in Fig.3a. The XRD pattern of prepared AZO without CAs indicated a sharp peak at ~ 35°, implying the directional growth of AZO, which confirms the columnar rod growth. As can be observed, the crystallinity of AZO changes slightly after adding the $C_6H_{17}N_3O_7$ to the bath solution. However, the $C_6H_{17}N_3O_7$ +H_2O_2 greatly increases the degree of crystallinity. To calculate the micro-strain and crystallite size related to diffraction peak broadening, the Williamson-Hall method was employed. The integral breadth of an XRD peak is determined by the integrated intensity divided by the maximum intensity. Hence, the observed peak broadening, denoted as B_o, can be expressed as [25]:

$$B_r = B_0 - B_i \tag{5}$$

where B_o, B_i, and B_r are the observed peak broadening (in radians), the instrumental broadening (in radians), and the broadening because of the small crystallite size and lattice strain, respectively. The broadening associated with small particle size can be described according to the Debye-Scherrer equation as [25]:

$$B_c = \frac{K\lambda}{t\cos\theta} \tag{6}$$

B_c represents the broadening, which is caused only by the small size of the crystallites. k denotes a constant whose value is determined by the shape of the particle, and it is generally considered to be equal to one. The t, θ, and λ are the crystallite size, the Bragg angle, and the wavelength of the incident X-ray beam (1.54 Å), respectively. According to the Williamson-Hall method, the broadening caused by lattice strain is expressed as follows [25]:

$$B_s = 4\varepsilon\tan\theta \tag{7}$$

where B_s, ε, and θ signify the peak broadening resulting from the lattice strain, the strain distribution throughout the material, and the Bragg angle, respectively. Therefore, the overall broadening of the peak is represented by the combination of Equations (6) and (7), excluding the instrumental broadening, which can be defined as [25]:

$$B_r = \frac{K\lambda}{t\cos\theta} + 4\varepsilon\tan\theta \tag{8}$$

For the observed diffraction peaks, plots with 4sinθ on the horizontal axis and βcosθ values on the vertical axis are drawn (Fig.3(b-d)). In the plot, the y-intercept corresponds to the crystallite size, and the slope of the linear fit reflects the lattice strain, which is shown in Fig.3e. As can be observed, the crystallite size increases by the addition of $C_6H_{17}N_3O_7$+H_2O_2 to the bath solution. Regarding the lattice strain, an enhancement is observed in comparison with two other conditions (without (W/O) CAs and $C_6H_{17}N_3O_7$-asisted growth). The increase in strain can be due to the narrow vertical rods that are tightly packed together (compared to the sample without the CAs) and to the higher thickness (compared to the $C_6H_{17}N_3O_7$-asisted growth). Also, the data obtained from Fig.3e are shown in Table 1. These issues will be discussed in the section on topography and microstructure examination by FESEM analysis.

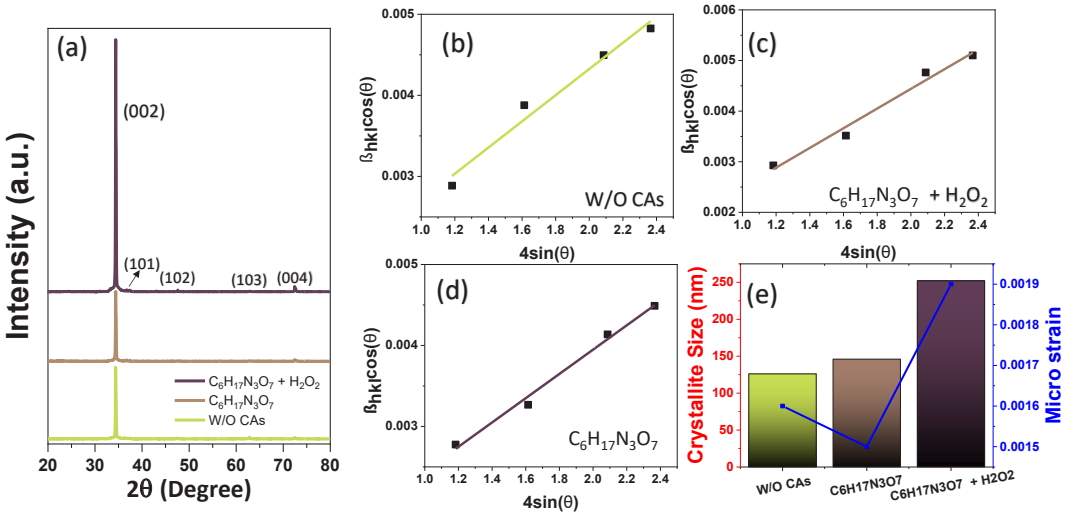

Fig. 3- (a) XRD patterns of the AZO layers (W/O CAs and with $C_6H_{17}N_3O_7$ as well as $C_6H_{17}N_3O_7$ +H_2O_2), (b-d) the Williamson-Hall plots, and (e) the corresponding micro strain and the crystallite size extracted from the Williamson-Hall method.

Table 1- Micro-strain and crystalline size obtained by the Williamson-Hall method

	Crystallite Size (nm)	Micro strain
W/O CAs	126 ∓ 0.5	$0.00161 \mp 1.8e-4$
$C_6H_{17}N_3O_7$	145 ∓ 0.5	$0.0015 \mp 1.0e-4$
$C_6H_{17}N_3O_7+H_2O_2$	252 ∓ 0.5	$0.0019 \mp 2.0e-4$

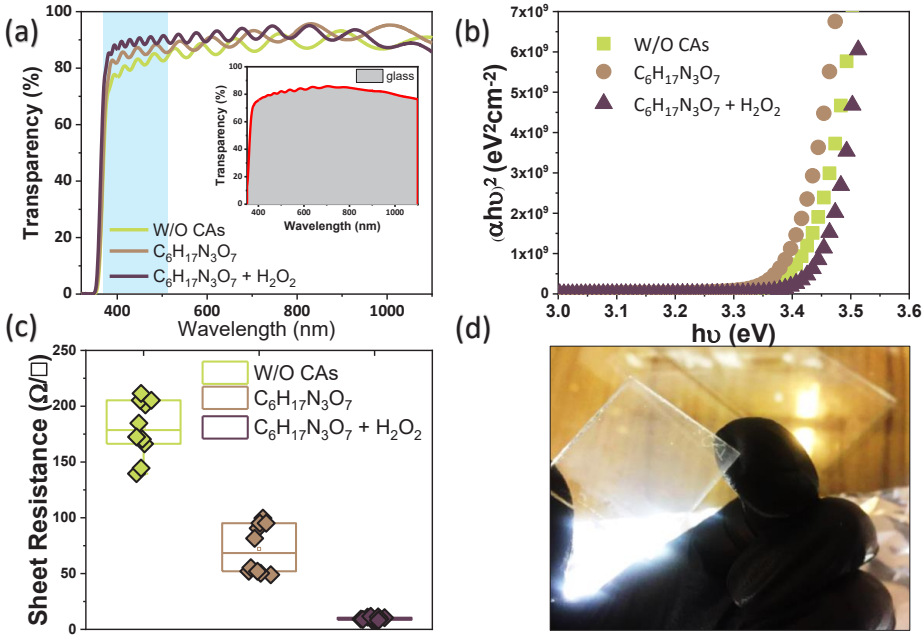

Fig. 4- (a) Light transmission spectra, (b) Tauc plot, (c) sheet resistance of AZO layers (without CAs, with $C_6H_{17}N_3O_7$ and $C_6H_{17}N_3O_7$+H_2O_2), and (d) the digital photos of AZO prepared with $C_6H_{17}N_3O_7$+H_2O_2.

The light transmission spectra of the as-prepared AZO layers without CAs and with $C_6H_{17}N_3O_7$, as well as $C_6H_{17}N_3O_7$ +H_2O_2, are shown in Fig.4a. The inset in this figure displays light transmission of ~80% for SLG for comparison. In addition, AZO prepared with $C_6H_{17}N_3O_7$ +H_2O_2 indicates higher light transmission than AZO fabricated with and without $C_6H_{17}N_3O_7$. Fig.4b displays the band gap of the as-prepared AZO layers. It can be seen that the AZO layers fabricated with $C_6H_{17}N_3O_7$ +H_2O_2, $C_6H_{17}N_3O_7$, and without $C_6H_{17}N_3O_7$ indicate a band gap of 3.45, 3.42, and 3.39 eV, respectively. It seems that altering the degree of crystallinity results in a change in the bandgap. Additionally, the Burstein–Moss shift occurs when an increased carrier concentration fills the lower states of the conduction band, thereby forcing optical transitions to higher energy levels. Consequently, the measured optical band gap appears larger than the material's intrinsic band gap [26]. The sheet resistance variation, as another important property of transparent conductive layers, is shown in Fig. 4c. As can be seen, the presence of the growth CAs has a significant effect on this parameter. The regular growth of hexagonal rods compared to the irregular growth leads to an increase in mobility and a decrease in electrical resistance. Calculating the carrier concentration or mobility by Hall effect measurements would greatly strengthen the claims regarding improved conductivity. However, due to limited access to this technique, it was not possible to examine the conductivity changes more closely. Fig.4d shows the camera picture of the AZO film prepared by $C_6H_{17}N_3O_7$ +H_2O_2, which exhibits remarkable transparency.

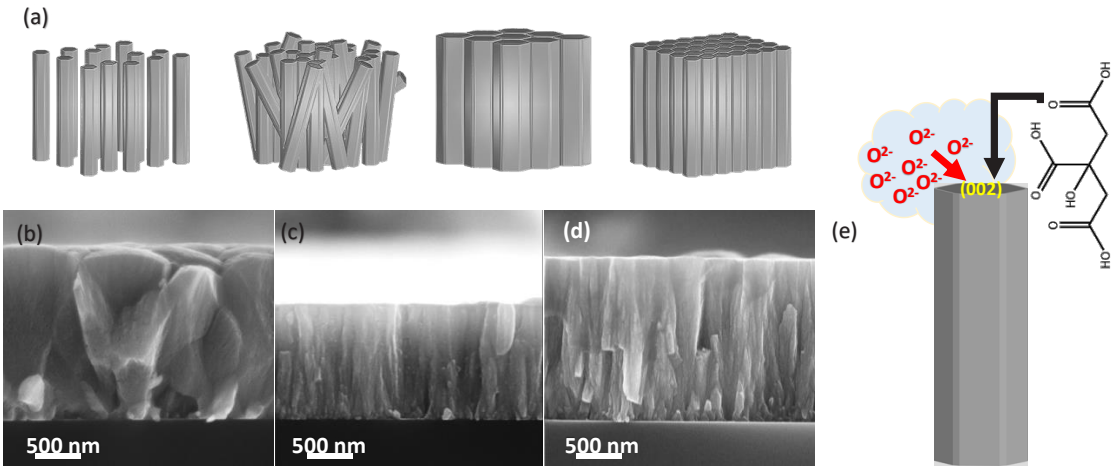

Fig. 5- (a) Schematic illustration of the different possible growth modes of AZO on the substrate during the CBD process, the cross-sectional FESEM images of AZO films (b) without CAs, (c) with $C_6H_{17}N_3O_7$, and (d) $C_6H_{17}N_3O_7$+H_2O, (e) the proposed formation mechanism of columnar growth of AZO with $C_6H_{17}N_3O_7$+H_2O_2.

Different possible growth conditions of AZO on the substrate are shown in Fig.5a. The form of the rods changes as the growing conditions change. In the first case, separate rods are seen in the structure and have a lower density, which is not suitable for AZO as a TCO. For the second item, the irregular, tangled, and tilted rod structures scatter the light and charge carriers, making it inappropriate in terms of the electro-optical properties required for TCO. In the third case, the rods are completely compact. In addition, they have a large width, which is not suitable in terms of transparency. Therefore, the thickness and orientation can change with changing growth conditions. In the latter item, by adding CAs, rods with a regular, dense, and thin structure are observed, which are very suitable for the optical and electrical properties of a TCO. As shown in Fig.5b, the irregular growth of AZO without CAs can be observed from the FESEM image. Adding $C_6H_{17}N_3O_7$ to the chemical bath leads to controlled and regular growth of rods (Fig.5c). Also, the increase in thickness of AZO structure is probably due to the binding of $Al(OH)_4^-$ ions around the formed rods. Furthermore, the diameter of the rods decreases, and the thickness decreases. Fig.5d indicates the cross-sectional FESEM image of the prepared AZO layer with $C_6H_{17}N_3O_7$ +H_2O_2 as CAs. Very regular and packed growth of AZO rods is observed. In addition, the diameter of the rods decreases in comparison with CAs free growth, and the thickness increases in comparison with $C_6H_{17}N_3O_7$-assisted growth. The thickness, optical transparency, sheet resistance, and resistivity of the fabricated AZO layers were compared in Table 2.

The possible growth mechanism of vertically aligned AZO can be suggested (Fig.5e) based on the previous study [27]. The AZO crystal typically possesses polar faces, such as the (002) plane, and non-polar faces, which include the (100) and (101) planes. Polar faces with surface dipoles exhibit lower thermodynamic stability compared to nonpolar surfaces, which typically undergo rearrangement to reduce surface energy. Hence, the growth rate along the (002) plane is more rapid compared to that in other directions. As a consequence of this polarity, the (002) face of the crystal can exhibit either a positive or a negative charge. In either case, the surface will attract ions with opposite charges, e.g., citrate ions. Also, the H_2O_2 is an oxidizing agent used as the source of oxygen. It seems that H_2O_2 is easily decomposed on the (002) AZO surface into H_2O and O_2. Then, O_2 is adsorbed on the catalyst surface, and the double bond between the oxygens is broken. In the final, chemisorption of oxygen with the AZO occurs, resulting in the growth of the crystallites along the polar (002) plane [27]. This newly ion-coated surface will subsequently attract additional ions of opposite charges, which will lead to the formation of AZO rods through a reactive process [27]. These results agree with XRD patterns.

Additionally, a comparison of other TCOs and their typical properties with as-prepared AZO with $C_6H_{17}N_3O_7$ +H_2O_2 is provided in Table 3.

Table 2- The thickness, optical transparency, sheet resistance, and resistivity of the fabricated AZO layers

sample	Thickness (μm)	Optical Transparency at 380 – 740 (%)	Sheet resistance ($\Omega\ \square^{-1}$)	Resistivity ($\Omega.cm$)
W/O CAs	1.9	84.7	180	3.4×10^{-2}
$C_6H_{17}N_3O_7$	1.2	87.9	72	8.6×10^{-3}
$C_6H_{17}N_3O_7 + H_2O_2$	1.8	90.4	10	1.8×10^{-3}

Table 3- The optical transparency and sheet resistance of TCO materials retrieved from the literature in comparison with the as-prepared AZO

Samples	Optical Transmittance (%)	sheet resistance ($\Omega\ \square^{-1}$)	Ref.
ITO (Indium Tin Oxide)	85-92	7-62	[28]
FTO (Fluorine-doped SnO_2)	80-91	7-164	[29-31]
AZO (Al-doped ZnO)	80-95	$2\text{-}3\times10^5$	[32-34]
This work	90.4	10	-

To compare this research with other literature, Iwantono et al. [35] prepared AZO rods via seed-mediated hydrothermal method at 90°C for 8 h. At different concentrations of $Al(NO_3)_3$ precursor, the thickness of AZO changed. At 2% of Al, the thickness of 1.903 μm was obtained. However, the AZO rods exhibited irregular growth. Fuchs et al. [36] fabricated AZO thin films at 100 ^{0}C via the CBD approach at various concentrations of $Al(NO_3)_3$ from 0.5-10 mM. Compact films with columnar grains were obtained using low concentrations of Al precursor. However, disturbance of the columnar growth occurred at concentrations of ~ 2mM $Al(NO_3)_3$. At higher concentrations, a platelet-like structure was formed instead of columnar growth, which resulted in increased resistivity ($\rho > 20\ \Omega.cm$). Affiqah Arzaee [37] et al. prepared AZO layer by the spin coating technique. The film thickness was controlled by changing the spin speed (3000 rpm) and the number of layers (3 layers). The as-prepared AZO layer showed transparency of 90% and the resistivity of $3.22 \times 10^3\ \Omega.cm$. Nevertheless, the optimized AZO layer showed a rougher surface than other as-fabricated layers. Henni et al. [38] prepared AZO via the electrodeposition method at different $Al(NO_3)_3$ precursors. The results showed that as Al concentration increased, the optical band gap also increased from 3.31 to 3.45 eV. In addition, the crystallinity of AZO films decreased by enhancing the dopant concentration. Furthermore, the structure of the AZO rods also grew irregularly, which affects the optical properties and electrical resistivity. In this work, employing CBD via H_2O_2 and $C_6H_{17}N_3O_7$ as CAs, accompanied by using $Al(OH)_3$ precursor, can effectively alter the morphology of AZO layers and their physical properties, which paves the way for their more efficient utilization in optoelectronic devices.

4. Conclusion

In summary, the vertically aligned AZO rods were grown onto an SLG substrate using the CBD technique with $C_6H_{17}N_3O_7$ and H_2O_2 as CAs. It is important to note that this approach is straightforward and allows for easy control of growth parameters. In general, the presence of $C_6H_{17}N_3O_7$ and H_2O_2 in the bath solution causes the under-growth rods to align predominantly along the (002) plane, resulting in the vertical growth of AZO. Therefore, the results showed that the simultaneous presence of $C_6H_{17}N_3O_7$ and H_2O_2 in the bath solution strongly affected the structural, morphological, and optical properties. The as-prepared AZO with $C_6H_{17}N_3O_7$ and H_2O_2 exhibited a layer thickness of 1.8 μm, optical transparency of 90.4 %, sheet resistance of 10 $\Omega\ \square^{-1}$, and the resistivity of $1.8 \times 10^{-3}\ \Omega.cm$.

References

1. E. Baghestani, F. Tajabadi, Z. Saki, M. Heidariramsheh, F. Ghasemi, S. Darbari, S. Mashhoun, N. Taghavinia, A conductive adhesive ink for carbon-laminated perovskite solar cells with enhanced stability and high efficiency, Solar Energy, 266 (2023) 112165.
2. M. Forouzandeh, M. Heidariramsheh, H.R. Heydarnezhad, H. Nikbakht, M. Stefanelli, L. Vesce, N. Taghavinia, Enhanced carbon-based back contact electrodes for perovskite solar cells: Effect of carbon paste composition on performance and stability, Carbon, 229 (2024) 119450.
3. A. Acharya, B. Sarwan, R. Panda, S. Shrivastava, V. Ganesan, Tuning of TCO properties of ZnO by silver addition, Superlattices and Microstructures, 67 (2014) 97-109.
4. E. Filatova, A. Baraban, A. Konashuk, M. Konyushenko, A. Selivanov, A. Sokolov, F. Schaefers, V. Drozd, Transparent-conductive-oxide (TCO) buffer layer effect on the resistive switching process in metal/TiO2/TCO/metal assemblies, New Journal of Physics, 16 (2014) 113014.
5. H. Sai, T. Koida, T. Matsui, Improved electrical contact properties in Indium-free silicon heterojunction solar cells with amorphous SnO2 TCO layers, Solar Energy Materials and Solar Cells, 278 (2024) 113191.
6. L. Kathwate, In-doped ZnO films deposited by modified SILAR method for enhanced ethanol gas sensor application, Ceramics International, 50 (2024) 48462-48473.
7. H.W. Lee, S. Biswas, H. Choi, Y. Lee, H. Kim, Improving photostability of non-fullerene acceptor-based inverted organic solar cells using Ga-doped ZnO electron transport layer, Applied Surface Science, 659 (2024) 159930.
8. S. Chowdhury, K.S. Lau, A.S. Najm, H.S. Naeem, A.M. Holi, N. Amin, A. Laref, M.S. Jamal, C.H. Chia, Structural, morphological, and optical properties of Al-doped ZnO Material synthesized via sol-gel and spin coating: Insights into crystallinity and doping effects, Materials Research Bulletin, 190 (2025) 113516.
9. Z. Li, A. Xie, Q. Nong, Y. Sun, H. Cai, Z. Chen, J. He, P. Gao, Boron-Doped Zinc Oxide Electron-Selective Contacts for Crystalline Silicon Solar Cells with Efficiency over 22.0%, Small Science, 4 (2024) 2400168.
10. E. Bacaksiz, S. Aksu, S. Yılmaz, M. Parlak, M. Altunbaş, Structural, optical and electrical properties of Al-doped ZnO microrods prepared by spray pyrolysis, Thin Solid Films, 518 (2010) 4076-4080.
11. M.F. Gözükızıl, PH effect on structural, morphological and optical properties of ZnO thin films produced by chemical bath deposition method, Eur Chem Bull, 9 (2020) 335-338.
12. H.Q. AL-Arique, S.S. AL-Qadasy, N.M. Kaawash, S. Chishty, K.A. Bogle, Study the characterization of ZnO and AZO films prepared by spray pyrolysis and the effect of annealing temperature, Optical Materials, 150 (2024) 115261.
13. G.-B. Lee, S.H. Song, M.-W. Lee, Y.-J. Kim, B.-H. Choi, Characterization of physical and mechanical properties of Al2O3-doped ZnO (AZO) thin films deposited on transparent polyimide supports with various ALD process parameters, Applied Surface Science, 535 (2021) 147731.
14. Y. Wang, G. Xu, J. Yang, W. Mao, J. Wang, Z. Liu, Y. Dong, S. Yang, J. Li, Fabrication of AZO and FAZO films using low-cost spin-coating method, Optical Materials, 126 (2022) 112204.
15. M. Heidariramsheh, H. Jalalichamani, M. Shabanzadeh, S.M. Mahdavi, N. Taghavinia, Comparison of meniscus-printed Cu2Sn (S, Se) 3 and Cu2ZnxSn (S, Se) 4 thin films to apply in superstrate solar cells, Materials Research Bulletin, 184 (2025) 113243.
16. M.K. Sahnesarayi, S. Rastegari, H. Sarpoolaky, Enhanced photoelectrochemical water splitting performance of vertically aligned Bi2O3 nanosheet arrays derived from chemical bath deposition method by controlling chemical bath temperature and complexing agent concentration, Surfaces and interfaces, 30 (2022) 101819.
17. M.C. Portillo, O.P. Moreno, R.G. Pérez, M.A. García, M.H. Hernández, S.S. Sauceda, F.M. Bustamante, R.R. Gutiérrez, Structural and optical properties of ZnO nanocrystals growth by the chemical bath deposition, Optik, 157 (2018) 125-133.
18. Z. Shi, A.V. Walker, Chemical bath deposition of ZnO on functionalized self-assembled monolayers: selective deposition and control of deposit morphology, Langmuir, 31 (2015) 1421-1428.
19. B. Cao, W. Cai, From ZnO nanorods to nanoplates: chemical bath deposition growth and surface-related emissions, The Journal of Physical Chemistry C, 112 (2008) 680-685.
20. R.S. Kumar, P. Sudhagar, R. Sathyamoorthy, P. Matheswaran, Y.S. Kang, Direct assembly of ZnO nanostructures on glass substrates by chemical bath deposition through precipitation method, Superlattices and Microstructures, 46 (2009) 917-924.
21. M. Szymańska-Chargot, J. Cieśla, M. Chylińska, K. Gdula, P.M. Pieczywek, A. Kozioł, K.J. Cieślak, A. Zdunek, Effect of ultrasonication on physicochemical properties of apple based nanocellulose-calcium carbonate composites, Cellulose, 25 (2018) 4603-4621.
22. S. Bose, C. Chevallier, S.O.S. Hamady, D. Horwat, J.-F. Pierson, P. Boulet, T. Gries, T. Aubert, N. Fressengeas, Elaboration of high-transparency ZnO thin films by ultrasonic spray pyrolysis with fast growth rate, Superlattices and Microstructures, 156 (2021) 106945.
23. C. Wang, H. Zhang, F. Yang, Y. Fan, Q. Liu, Enhanced light scattering effect of wrinkled transparent conductive ITO thin film, RSC Advances, 7 (2017) 25483-25487.
24. Y.-T. Cheng, T.-L. Lu, M.-H. Hong, J.-J. Ho, C.-C. Chou, J. Ho, T.-P. Hsieh, Evaluation of transparent ITO/nano-Ag/ITO electrode grown on flexible electrochromic devices by roll-to-roll sputtering technology, Coatings, 12 (2022) 455.
25. R. Zamiri, B. Singh, M.S. Belsley, J. Ferreira, Structural and dielectric properties of Al-doped ZnO nanostructures, Ceramics International, 40 (2014) 6031-6036.
26. S. Lee, Q. Wang, V. Chakrapani, Interplay of surface transfer doping and Burstein Moss shift in V 2 O 5/V 2 O 5–x: Implications for band gap, doping, and catalysis, Physical Review Materials, 9 (2025) 085801.
27. K. Gurav, U. Patil, S. Pawar, J. Kim, C. Lokhande, Controlled crystallite orientation in ZnO nanorods prepared by chemical bath deposition: Effect of H2O2, Journal of Alloys and Compounds, 509 (2011) 7723-7728.
28. Kim, K. H., Koo, B. R., & Ahn, H. J. Sheet resistance dependence of fluorine-doped tin oxide films for high-performance electrochromic devices. Ceramics International, 44(8) (2018) 9408-9413.
29. J.H. Park, D.J. Byun, J.K. Lee, Electrical and optical properties of fluorine-doped tin oxide (SnOx: F) thin films deposited on PET by using ECR–MOCVD, Journal of electroceramics, 23 (2009) 506-511.
30. A. Way, J. Luke, A.D. Evans, Z. Li, J.-S. Kim, J.R. Durrant, H.K. Hin Lee, W.C. Tsoi, Fluorine doped tin oxide as an alternative of indium tin oxide for bottom electrode of semi-transparent organic photovoltaic devices, AIP Advances, 9 (2019).
31. Z.Y. Banyamin, P.J. Kelly, G. West, J. Boardman, Electrical and optical properties of fluorine doped tin oxide thin films prepared by magnetron sputtering, Coatings, 4 (2014) 732-746.
32. F. Wang, M. Wu, Y. Wang, Y. Yu, X. Wu, L. Zhuge, Influence of thickness and annealing temperature on the electrical, optical

and structural properties of AZO thin films, Vacuum, 89 (2013) 127-131.
33. W.-J. Jeong, G.-C. Park, Electrical and optical properties of ZnO thin film as a function of deposition parameters, Solar Energy Materials and Solar Cells, 65 (2001) 37-45.
34. L. Li, S. Gao, P. Yang, Inducing efficient photoelectric properties at AZO/Ag/AZO nanomultilayer films, Crystal Growth & Design, 24 (2024) 2075-2081.
35. I. Iwantono, P. Nurrahmawati, S. Natalia, R.F. Syahputra, A. Awitdrus, Z. Zulkarnain, A.A. Umar, Aluminium Doping for Enhancing Charge Photoanode ZnO Nanorod for DSSC, International Journal of Nanoelectronics & Materials, 13 (2020).
36. P. Fuchs, H. Hagendorfer, Y.E. Romanyuk, A.N. Tiwari, Doping strategies for highly conductive Al-doped ZnO films grown from aqueous solution, physica status solidi (a), 212 (2015) 51-55.
37. N.A. Arzaee, F.I. Za'abar, M.S. Bahrudin, A.Z. Arsad, N.I. Azman, M.N. Abd Rahman, W.S. Wan Abdullah, C.F. Chau, A.W. Mahmood Zuhdi, Systematic optimization of sol–gel processed Al-doped ZnO for cost-effective transparent conductive oxide, Journal of Sol-Gel Science and Technology, 110 (2024) 52-61.
38. A. Henni, A. Merrouche, L. Telli, A. Karar, Studies on the structural, morphological, optical and electrical properties of Al-doped ZnO nanorods prepared by electrochemical deposition, Journal of Electroanalytical Chemistry, 763 (2016) 149-154.